Received: 8 October 2022 | Accepted: 21 December 2022

DOI: 10.1002/pamm.202200237

Global Stability Analysis of the Interaction Between a Longitudinal Vortex and an Oblique Shock Wave

Michael Werner[1,*] and **Stefan Hein**[1]

[1] German Aerospace Center - Institute for Aerodynamics and Flow Technology

In this study, the interaction of a longitudinal vortex with an oblique shock was studied numerically. A global stability approach was used to investigate the onset of unsteadiness due to vortex breakdown. For this purpose, steady and unsteady laminar flow simulations were performed. A longitudinal vortex with an exponentially decaying tangential velocity profile, a so-called Erlebacher vortex, was introduced into the flow field by a modification of the inflow boundary, while the oblique shock was created by a ramp in supersonic flow. Parametric studies concerning the influence of the axial velocity deficit and the tangential velocity component on the stability of the vortex were performed. Several amplified global eigenmodes could be identified and it could be shown that the frequencies predicted by the global stability analysis were in reasonable agreement with dominant frequencies observed in the unsteady simulations.

1 Introduction

Vortices and swirling flows in general play an important role in a broad range of natural and technical flows. In aerodynamics, leading edge vortices on delta wing aircraft have been a primary area of study for decades. Under certain flow conditions, an abrupt change in the flow topology can be observed, the so-called vortex breakdown. This phenomenon can greatly affect the aerodynamic performance of the aircraft, reducing the lift and, if it occurs asymmetrically, inducing strong moments that can compromise the stability and control of the aircraft. Vortex breakdown is typically connected to the development of a stagnation point in the vortex core, followed by an area of reversed flow [11]. For incompressible vortices, vortex breakdown typically occurs once a critical swirl ratio S is exceeded [13]. However, for vortices in supersonic flow vortex breakdown can also be caused by the interaction with a shock wave [10]. Most numerical studies of shock-induced vortex breakdown are based on conventional simulations solving the Euler or the Reynolds-averaged Navier-Stokes (RANS) equations. One example is the work of Thomer et al., who performed extensive studies concerning the interaction between a longitudinal vortex and normal or oblique shocks [21, 22]. The interaction between a longitudinal vortex and an oblique shock caused by a ramp was studied by Magri et al. [14]. They found breakdown characteristics similar to those found in subsonic flows. Another approach is to view vortex breakdown as a stability problem. For incompressible flows, linear stability theory has long been used to study the stability of vortices [12, 19]. However, local linear stability analysis assumes negligible gradients in the direction of flow. In the area around a shock this assumption is invalid. An alternative approach is the use of global linear stability analysis (GSA). In contrast to local linear stability analysis, no assumptions about the spatial structure of the instability are made. It was first applied by Pierrehumbert and Widnall to shear layer instabilities [17]. Most of the early studies focused on fundamentally two-dimensional flows, such as cavity flows or the wake behind a cylinder [20]. By studying the two-dimensional turbulent flow around a NACA0012 profile, Crouch et al. could show that the onset of shock buffet is also caused by a global instability [3]. In recent years, due to the increase in available computational resources, it also became possible to study fully three-dimensional flows. With regard to vortex breakdown, most studies focused on incompressible vortices. Meliga and Gallaire [16] analyzed spiral vortex breakdown based on direct numerical simulation (DNS) results. They performed a global stability analysis in the region of the breakdown bubble and found that spiral vortex breakdown is caused by an unstable eigenmode. Qadri et al. [18] also studied spiral vortex breakdown and could confirm the findings of Meliga and Gallaire. Additionally, they extended the approach to calculate the structural sensitivity in order to identify the wavemaker region responsible for the spiral vortex breakdown.

In this paper, the applicability of the global stability analysis to compressible flows with shock is investigated. For this reason, a matrix-forming three-dimensional global stability analysis approach will be used to detect and study the onset of unsteadiness due to vortex breakdown of a longitudinal vortex caused by the interaction with an oblique shock. Additionally, comparisons with unsteady laminar flow simulations are used to validate the applicability of this approach for the study of vortex-shock interactions.

* Corresponding author: e-mail michael.werner@dlr.de,

2 Global Stability Analysis

2.1 Theoretical Formulation

The theoretical formulation of the global stability analysis is based on the approach outlined e.g. by Iorio et al. [8]. The general form of the finite volume formulation of the Navier-Stokes equations can be given in compact form as

$$\mathbf{B}\frac{\partial q(x,y,z,t)}{\partial t} = \mathbf{R}(q(x,y,z,t)), \tag{1}$$

where $\mathbf{B}$ is a diagonal matrix containing the cell volumes, q are the base flow variables and $\mathbf{R}$ is the residual. To linearize the equation, a decomposition of the base flow variables q into the steady base flow Q and a small perturbation q' is introduced:

$$q(x,y,z,t) = Q(x,y,z) + \epsilon q'(x,y,z,t), \tag{2}$$

where $\epsilon \ll 1$. By combining the equations 1 and 2 and subsequent linearization, we arrive at

$$\mathbf{B}\frac{\partial Q(x,y,z)}{\partial t} + \epsilon\mathbf{B}\frac{\partial q'(x,y,z,t)}{\partial t} = \mathbf{R}(Q(x,y,z)) + \epsilon\mathbf{R}(q'(x,y,z,t)), \tag{3}$$

which can be simplified to

$$\epsilon\mathbf{B}\frac{\partial q'(x,y,z,t)}{\partial t} = \epsilon\mathbf{R}(q'(x,y,z,t)), \tag{4}$$

as we assume a fully converged steady base flow, $\partial Q(x,y,z)/\partial t = 0$ and $\mathbf{R}(Q(x,y,z)) = 0$.
In the next step, a harmonic ansatz in time is chosen for the perturbation:

$$q'(x,y,z,t) = \hat{q}(x,y,z) \cdot e^{-\omega t}, \tag{5}$$

where $\hat{q}$ is the complex-valued eigenvector and ω is a complex-valued eigenvalue. By inserting equation 5 into equation 4 we obtain:

$$-\omega\mathbf{B}\hat{q} \cdot e^{-\omega t} = \left[\frac{\partial \mathbf{R}}{\partial q}\right]_Q \hat{q} \cdot e^{-\omega t}. \tag{6}$$

With $\mathbf{A} = \left[\frac{\partial \mathbf{R}}{\partial q}\right]_Q$ as the Jacobian of the steady base flow we get:

$$\mathbf{A}\hat{q} = -\omega\mathbf{B}\hat{q} \tag{7}$$

This generalized eigenvalue problem is then solved by using a Krylov subspace approach to find the eigenvalues $\omega = \omega_r + i\omega_i$ and eigenvectors $\hat{q}$. The resulting eigenvectors correspond to the spatial structure of the global instabilities, whereas the real and the imaginary part of the eigenvalues can be interpreted as its damping rate and dimensionless frequency, respectively. The damping rate, ω_r, determines whether the corresponding instability is damped, $\omega_r \geq 0$, or amplified, $\omega_r < 0$.

2.2 Solution of the Generalized Eigenvalue Problem

The method outlined in section 2.1 was implemented in the scope of the DLR FlowSimulator framework [15]. This framework serves as an interface between the DLR TAU code [6] and a collection of Python libraries used to control the simulations and access the generated data. The Jacobian was computed on the same computational grid as the base flow. The discrete formulation of the Jacobian was previously derived by Dwight [4]. For the solution of the generalized eigenvalue problem a combination of the numerical libraries PETSc [1] and SLEPc [7] was used. A Krylov-Schur eigensolver was chosen because its efficient restarting technique, together with a shift-and-invert approach, allowed for an efficient identification and extraction of the relevant eigenvalues. For the solution of the inner iterations of the linear system, an efficient BGCRO-DR solver was used [9]. Since the resulting system was generally ill-conditioned, an ILU(0) approach was used as a preconditioner. The convergence behaviour of the inner iterations was further improved by using a specifically built preconditioning matrix $\mathbf{P} = \alpha\mathbf{A}^{2nd} + (1-\alpha)\mathbf{A}^{1st}$. Here, α is a blending factor and $\mathbf{A}^{1st}$ and $\mathbf{A}^{2nd}$ are Jacobians with different levels of fill. For $\mathbf{A}^{1st}$ a first-order stencil was used, that only included the contribution of the nearest neighbors of each point, whereas $\mathbf{A}^{2nd}$ was built using a second-order stencil. For the current study, a blending factor of $\alpha = 0.5$ was used.

3 Case Setup

In the following section, the geometry of the computational domain and the relevant flow conditions will be presented. Additionally, information about the numerical schemes used for the base flow simulations will be given.

3.1 Geometry and Flow Conditions

In order to allow for direct control of the shock-vortex interaction and to avoid unnecessary disturbances introduced by a vortex generator geometry, a simplified setup was chosen for this study: the longitudinal vortex was introduced into the flow by a modification of the inflow boundary condition, and the oblique shock is generated by a ramp in supersonic flow. A sketch of the setup is given in Fig. 1. The resulting shock-vortex interaction is defined by several interaction parameters. On the one hand, the shock itself is influenced mainly by the free stream Mach number M and the ramp angle θ. On the other hand, the most important parameters of the longitudinal vortex are its circulation Γ_0, the axial velocity deficit δ and the vortex radius r_0. During this study, both the ramp angle $\theta = 11.5°$ and the free stream Mach number $M = 1.48$ were kept constant, leading to a shock of constant strength for all simulations. The Reynolds number based on the vortex diameter, $d_0 = 2r_0$, was set to $Re_{d_0} = 5 \cdot 10^5$ for all simulations.

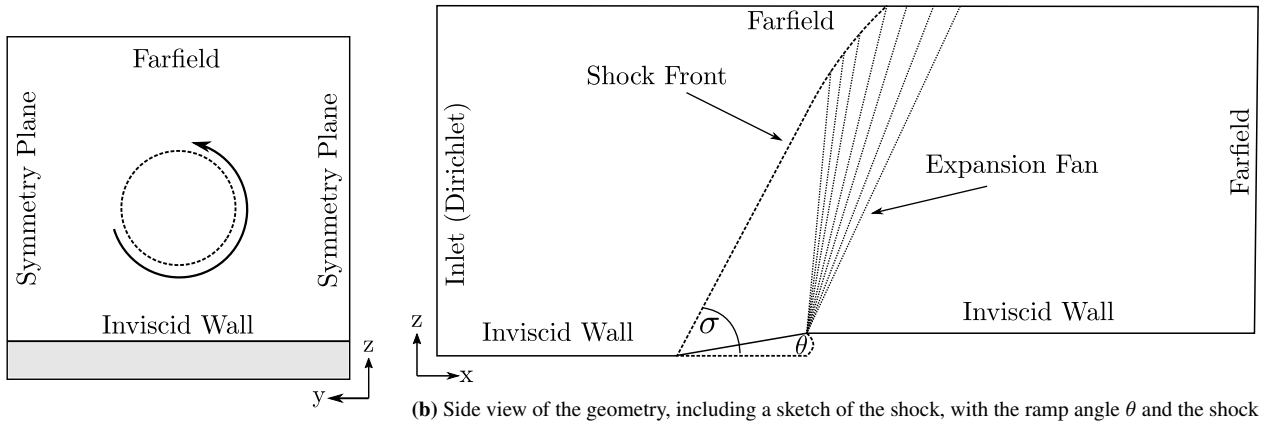

(a) Frontal view of the geometry.

(b) Side view of the geometry, including a sketch of the shock, with the ramp angle θ and the shock angle σ.

Fig. 1: Sketch of the computational domain.

In order to avoid an interaction between the vortex and domain boundaries, especially the solid walls of the ramp, an exponentially decaying vortex model originally proposed by Erlebacher et al. [5] was chosen. The axial and tangential velocity components at the inflow boundary, u and v_φ, respectively, are given as

$$u = U_\infty \left(1 - \delta e^{-r^{*2}}\right), \quad v_\varphi = \frac{\Gamma_0 r^*}{2\pi} e^{\frac{1-r^{*2}}{2}}, \tag{8}$$

with $\Gamma_0 = 2\pi r^* v_{\varphi,max}$, $r^* = r/r_0$, and $\delta = 1 - u_{center}/U_\infty$ as the velocity deficit in the vortex core. The vortex core radius r_0 is defined by the position of the maximum azimuthal velocity $v_{\varphi,max}$. Pressure and density at the inlet boundary were calculated by assuming isenthalpic flow. By varying Γ_0 and δ it is possible to affect the stability of the vortex interaction. Increasing Γ_0 or δ has a destabilizing effect, whereas decreasing these parameters stabilizes the vortex [21]. For this study, only vortices with a wake-type core, $\delta > 0$, were considered.

3.2 Numerical Solution Scheme

All computations of the base flow were carried out with the DLR TAU code [6], a three-dimensional finite volume code for the solution of the Navier-Stokes equations on hybrid-unstructured meshes. Previous numerical studies found a strong influence of the turbulence model on shock-induced breakdown [10]. To avoid additional uncertainties, a fully laminar approach was chosen for the present study. The spatial discretization of the laminar Navier-Stokes equations was achieved with a second-order central-differencing scheme, coupled with artificial matrix dissipation. A backward-Euler scheme was used for the temporal discretization, together with either a local time-stepping approach for the steady simulations, or a dual time-stepping approach for the unsteady simulations.

The mesh used in this study was created with the CENTAUR mesh generation software [2]. It was a fully hexahedral mesh with approximately $31 \cdot 10^6$ nodes. A simple mesh convergence study was carried out to determine cell sizes necessary to correctly resolve the occurring flow features. In the final mesh, isotropic cells with $\Delta x = \Delta y = \Delta z = 0.05 r_0$ were used in an area of $\pm 6 r_0$ around the vortex axis. To better capture the shock, the streamwise dimension of the cells was reduced to a minimum of $\Delta x = 0.015 r_0$ in the area above the ramp. While the base flow computations were mesh-converged, the global stability analysis proved to be more sensitive to the mesh resolution. However, with the available computational resources, no further refinement of the mesh was possible. Therefore, the results of the global stability analysis are not completely mesh-converged. As mentioned previously, the vortex was introduced by a modification of the inflow boundary. This was achieved by using a Dirichlet-type boundary condition, where the values of the flow variables could be explicitly specified at each point of the mesh. Both the ramp and the side walls in y-direction were modeled as inviscid walls. Finally, a non-reflective farfield condition was used for the upper boundary and the downstream boundary.

4 Numerical Results

4.1 Base Flow Simulations

In order to identify suitable flow conditions for the global stability analysis, a parametric study concerning the effect of the vortex parameters Γ_0 and δ was performed. As a result of this study, three different flow conditions with axial velocity deficits between $0.2 \leq \delta \leq 0.4$ were defined. The onset of vortex breakdown is strongly influenced by both Γ_0 and δ. As only flow conditions close to the onset of unsteadiness were of interest, both parameters had to be varied at the same time. The flow topology of the respective base flows was qualitatively similar for all investigated cases. In Fig. 2, the x-velocity component of the steady base flow, u, is shown for one case, $\Gamma_0 = 2.7, \delta = 0.3$. It can be seen that the shock/vortex interaction leads to a strong deformation of the shock front and the formation of a recirculation bubble in the vortex core downstream of the shock. Further downstream, the vortex interacts with the expansion fan at the end of the ramp, which leads to restabilization of the vortex. With increasing circulation or axial velocity deficit, the size of the area of reversed flow increases and the minimum velocity further decreases. It is worth noting that the existence of reversed flow in the vortex core is not sufficient to cause unsteadiness. Only after passing a certain threshold that depends on the vortex parameters Γ_0 and δ, the flow becomes unsteady. For two of the considered test cases, $\Gamma_0 = 2.7.\delta = 0.3$ and $\Gamma_0 = 3.68, \delta = 0.2$, unsteady flow simulations were carried out. In order to identify the onset of unsteadiness, time-series of the pressure in the vortex core downstream of the ramp were recorded. For the case $\Gamma_0 = 2.7.\delta = 0.3$, the dominant frequency of the resulting pressure fluctuations was $f = 112\,\mathrm{Hz}$, whereas the dominant frequency of the case $\Gamma_0 = 3.68, \delta = 0.2$ was $f = 163\,\mathrm{Hz}$.

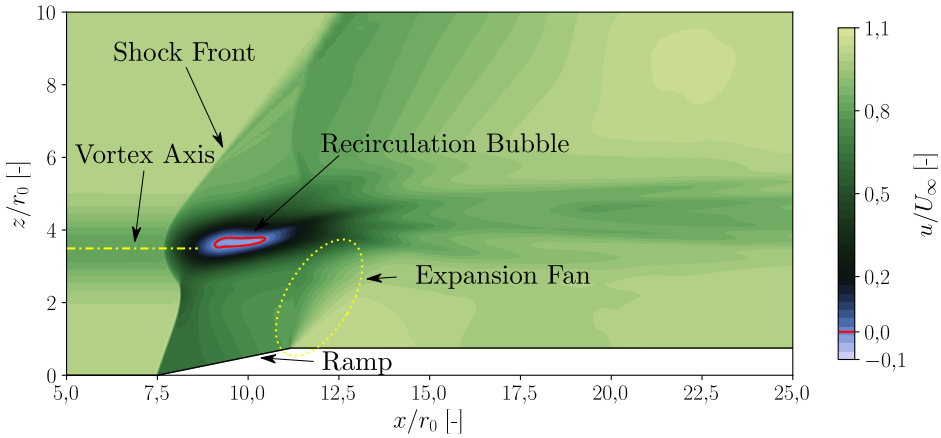

Fig. 2: Distribution of the normalized x-velocity component u/U_∞ of the steady base flow, $M = 1.48, \Gamma_0 = 2.7, \delta = 0.3$.

4.2 Global Stability Analysis

Based on the steady base flow computations presented in the previous section, the global stability analysis was performed for three different parameter combinations, $\Gamma_0 = 1.65, \delta = 0.4$, $\Gamma_0 = 2.7, \delta = 0.3$ and $\Gamma_0 = 3.68, \delta = 0.2$. The corresponding eigenvalue spectra are shown in Fig. 3. For each of the investigated cases, at least one amplified eigenvalue could be identified. It can be seen that by increasing the axial velocity deficit from $\delta = 0.2$ to $\delta = 0.4$, the dimensionless frequency of the most amplified eigenmode is decreased from $\omega_i = 0.16$ to $\omega_i = 0.039$. This observation is in good agreement with results of

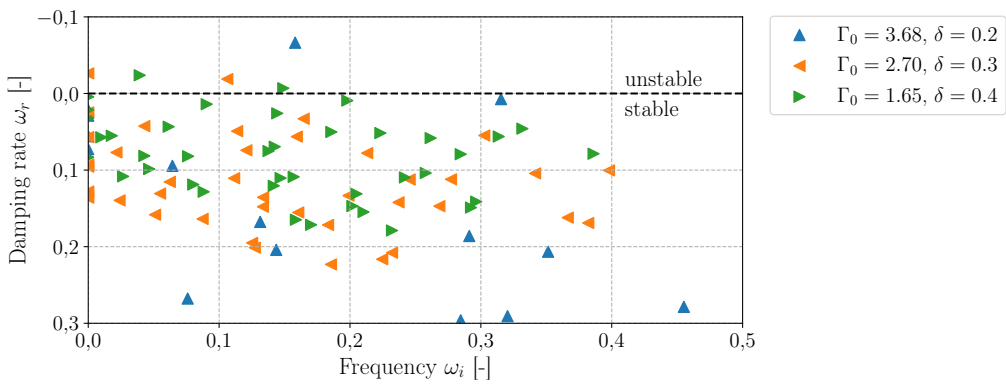

Fig. 3: Influence of the circulation Γ_0 and the axial velocity deficit δ on the computed eigenvalue spectrum.

unsteady flow simulations. For the case $\Gamma_0 = 2.7, \delta = 0.3$, the most amplified eigenvalue is $\omega = -0.019 + 0.106i$. Together with the internal reference velocity of the TAU code, $v_{ref} = 244.7\,\mathrm{m\,s^{-1}}$ and the reference length $l_{ref} = 2 * r_0 = 0.04\,\mathrm{m}$, the resulting frequency of the eigenmode is $f_{GSA} = (\omega_i v_{ref})/(2\pi l_{ref}) = 103\,\mathrm{Hz}$, as compared to the frequency of pressure oscillations of the URANS simulation, $f_{URANS} = 112\,\mathrm{Hz}$. Similarly, for the case $\Gamma_0 = 3.68, \delta = 0.2$ the stability analysis predicts a frequency of $f_{GSA} = 153\,\mathrm{Hz}$, compared to a frequency of $f_{URANS} = 163\,\mathrm{Hz}$ based on unsteady simulations. For both cases, the frequency predicted by the global stability analysis is approximately $5 - 10\%$ too low. Discrepancies of a similar magnitude were also reported for different applications of the global stability analysis [3], where they were attributed to non-linear effects in the flow field. Also, the results of the global stability analysis are not completely mesh-converged, as was mentioned in section 3.2, which might explain at least a part of the observed differences in frequency.

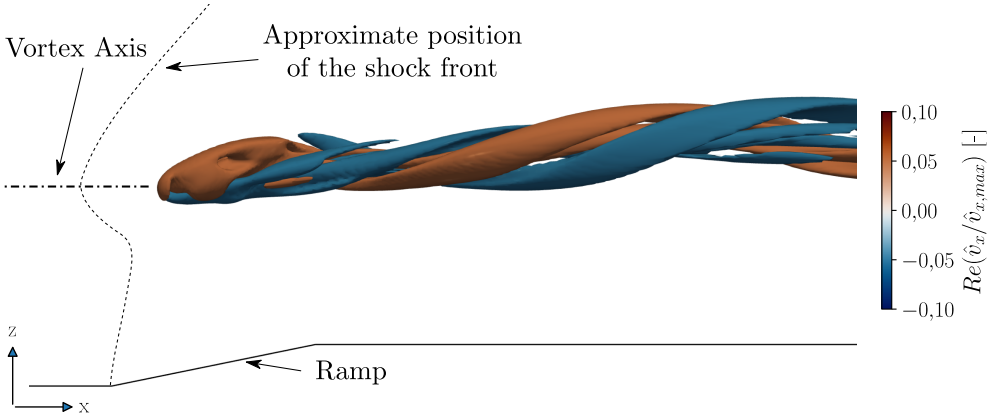

Fig. 4: Shape of the most amplified eigenmode, visualized by two iso-surfaces of the real part of the x-velocity mode $\hat{v}_x, \Gamma_0 = 2.7, \delta = 0.3$.

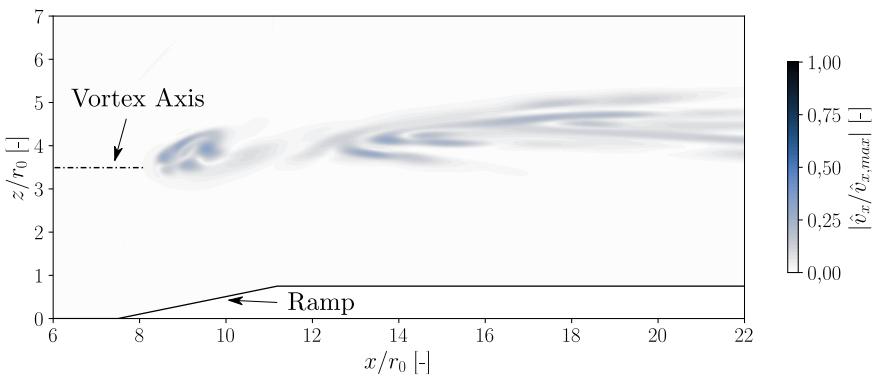

(a) Distribution of the normalized x-velocity component $\hat{v}_x/\hat{v}_{x,max}$ of the eigenvector.

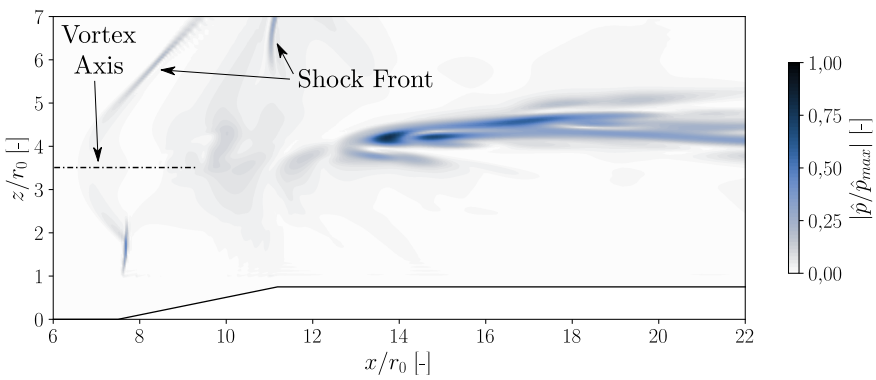

(b) Distribution of the normalized pressure component $\hat{p}/\hat{p}_{max}$ of the eigenvector.

Fig. 5: Visualization of the eigenvectors of the most amplified eigenmode, $\Gamma_0 = 2.7, \delta = 0.3$.

The eigenvectors of the computed eigenmodes feature a complex three-dimensional shape. This can be seen in Fig. 4, where two iso-surfaces of the x-velocity component of the most amplified eigenmode for the case $\Gamma_0 = 2.7, \delta = 0.3$ are

plotted. The iso-surfaces originate from the area of reversed flow above the ramp and spiral around each other with the same rotational direction as the base flow vortex. In order to compare the eigenfunctions of different flow variables, Fig. 5 shows y-normal cut sections along the vortex axis for the case $\Gamma_0 = 2.7, \delta = 0.3$. In Fig. 5a, the x-velocity component of the most amplified eigenmode is plotted. Here, the highest amplitudes are found in the area of the recirculation bubble above the ramp and in the vortex core downstream of the ramp. Generally, the amplitudes are limited to the area of the vortex core in the base flow simulations. In contrast, Fig. 5b shows the eigenvector corresponding to the pressure. Here, the highest amplitudes are found in the vortex core downstream of the ramp and along the shock front, which suggests the occurence of shock oscillations due to vortex breakdown.

5 Conclusions

This paper presents a numerical study of the interaction between a longitudinal vortex and an oblique shock at $M = 1.48$. The focus of the current work was the application of a global stability analysis to study the shock-vortex interaction. To this end, conventional steady and unsteady laminar flow simulations were performed to identify suitable conditions close to the onset of unsteadiness due to vortex breakdown. Based on these simulations, a fully three-dimensional global stability analysis was performed for several vortices with varying levels of circulation and axial velocity deficit. For each of the investigated flow conditions at least one amplified global eigenmode could be identified. The corresponding eigenvectors featured a complex three-dimensional shape. The highest amplitudes for the velocity components were found in the area of reversed flow above the ramp, whereas the highest amplitudes of pressure and density occurred in the vortex core downstream of the ramp and along the shock front.

A simple mesh convergence study with three different meshes showed that the results of the global stability analysis were not completely mesh-converged. While the eigenvalues of the most amplified eigenmode still varied between the medium and fine mesh, the corresponding eigenvectors were qualitatively similar. However, due to the large memory requirements of the applied approach, no further mesh refinement was possible with the available computational resources.

A comparison of the results of the global stability analysis with results of unsteady simulations showed a good agreement with regard to the onset of unsteadiness between both approaches. However, it was also shown that the frequencies predicted by the stability analysis were between $5 - 10\%$ too low compared to the results of the unsteady simulations.

Acknowledgements The authors gratefully acknowledge the Gauss Centre for Supercomputing e.V. (www.gauss-centre.eu) for helping to fund this project by providing computing time on the GCS Supercomputer SuperMUC-NG at Leibniz Supercomputing Centre (www.lrz.de). Open access funding enabled and organized by Projekt DEAL.

References

[1] S. Balay, W. D. Gropp, L. C. McInnes, B. F. Smith, Modern Software Tools for Scientific Computing, pp. 163–202 (1997).
[2] CentaurSoft, Online User's Manual - CENTAUR V15.0. URL: https://www.centaursoft.com (2021).
[3] J. D. Crouch, A. Garbaruk, D. Magidov, J. Comput. Phys.**224**, pp. 924–940 (2007).
[4] R. P. Dwight, Efficiency Improvements of RANS-Based Analysis and Optimization Using Implicit and Adjoint Methods on Unstructured Grids, PhD thesis, University of Manchester (2005).
[5] G. Erlebacher, M. Y. Hussaini, C.-W. Shu, J. Fluid Mech. **337**, pp. 129–153 (1997).
[6] T. Gerhold, MEGAFLOW - Numerical Flow Simulation for Aircraft Design, pp. 81–92 (2005).
[7] V. Hernandez, J. E. Roman, V. Vidal, ACM Trans. Math. Software **31**, pp. 351–362 (2005).
[8] M. C. Iorio, L. M. Gonzalez, E. Ferrer, Int. J. Numer. Methods Fluids **76**, p. 22 (2014).
[9] P. Jolivet, P.-H. Tournier, SC16: International Conference for High Performance Computing, Networking, Storage and Analysis, Salt Lake City, Utah (2016).
[10] I. M. Kalkhoran, M. K. Smart, Prog. Aerosp. Sci. **36**, pp. 63–95 (2000).
[11] S. Leibovich, Annu. Rev. Fluid Mech. **10**, pp. 221–246 (1978).
[12] M. Lessen, P. J. Singh, F. Paillet, J. Fluid Mech. **63**, pp. 753–763 (1974).
[13] O. Lucca-Negro, T. O'Doherty, Prog. Energy Combust. Sci. **27**, pp. 431–481 (2001).
[14] V. Magri, I. M. Kalkhoran, Comput. Fluids **86**, pp. 343–356 (2013).
[15] M. Meinel, PARA 2010, Reykjavik, Island (2010).
[16] P. Meliga, F. Gallaire, 6th AIAA Theoretical Fluid Mechanics Conference, Honolulu, Hawaii, AIAA 2011-3604 (2011).
[17] R. T. Pierrehumbert, S. E. Widnall, J. Fluid Mech. **114**, p. 59 (1982).
[18] U. A. Qadri, D. Mistry, M. P. Juniper, J. Fluid Mech. **720**, pp. 558–581 (2013).
[19] R. Spall, AIAA 24th Fluid Dynamics, Plasmadynamics, and Lasers Conference, Orlando, Florida, AIAA 93-3034 (1993).
[20] V. Theofilis, Annu. Rev. Fluid Mech. **43**, pp. 319–352 (2011).
[21] O. Thomer, W. Schröder, E. Krause, Proceedings of International Conference RDAMM, Novosibirsk, Russia, pp. 737–749 (2001).
[22] O. Thomer, M. Klaas, W. Schröder, E. Krause, Computational Fluid and Solid Mechanics, pp. 1156–1159 (2003)

